In-Situ Pulsed Hydrogen Implantation in Atom Probe Tomography

Jean-Baptiste Maillet, Gerald da Costa, Benjamin Klaes, Christian Bacchi, Antoine Normand, Charly Vaudaulon, François Vurpillot

In-Situ Pulsed Hydrogen Implantation in Atom Probe Tomography

Jean-Baptiste Maillet[1], Gerald Da Costa[1], Benjamin Klaes[1], Christian Bacchi[1], Antoine Normand[1], Charly Vaudaulon[1], François Vurpillot[1]

[1]Univ Rouen Normandie, INSA Rouen Normandie, CNRS, Normandie Univ, GPM UMR 6634, F-76000 Rouen, France

Abstract

The investigation of hydrogen in atom probe tomography appears as a relevant challenge due to its low mass, high diffusion coefficient and presence as a residual gas in vacuum chambers, resulting in multiple complications for atom probe studies. Different solutions were proposed in the literature like ex-situ charging coupled with cryotransfer or H charging at high temperature in a separate chamber. Nevertheless, these solutions often faced challenges due to the complex control of specimen temperature during hydrogen charging and subsequent analysis. In this paper, we propose an alternative route for in-situ H charging in atom probe derived from a method developed in field ion microscopy. By applying negative voltage nanosecond pulse on the specimen in an atom probe chamber under low pressure of $H_{2,}$ it is demonstrated that high dose of H can be implanted in the range 2-20 nm beneath the specimen surface. An atom probe chamber was modified to enable direct negative pulse application with controlled gas pressure, pulse repetition rate and pulse amplitude. Through electrodynamical simulations, we show that the implantation energy falls within the range 100 - 1,000 eV and a theoretical depth of implantation was predicted and compared to experiments.

Key words: Atom Probe Tomography, Hydrogen, Storage, Implantation, Atomic Scale Characterization

Introduction

The study and analysis of hydrogen (H) in atom probe tomography (APT) remain a challenge today. H can embrittle most of materials as this low-mass atom diffuses into the bulk and is trapped by atomic defects such as vacancies, interstitial sites, dislocations, or grain boundaries (Lin et al., 2020) (Tweddle et al., 2021) (Chen et al. 2020) (So et al., 2009). The consequences include decohesion along the crystallographic planes (Sofronis, 2006) and decrease of the material ductility (Barrera et al., 2018). Hydrogen embrittlement (HE) can be proved and measured with tensile tests (Koyama et al., 2017). To mitigate HE, numerous studies have explored trapping sites of H in steels (Bhadeshia, 2016). Investigations on materials introducing trapping sites have also been conducted. Given the the nanometric scale required for characterizing these trapping sites, such as TiC or V_4C_3 for example, studies necessitate atomic-scale investigations. Atom probe tomography emerges as an ideal candidate, enabling the spatial 3D localization of H at the atomic scale, a capability which is not achievable with other techniques (Gault et al., 2021). Recent studies have shown that the introduction of trapping sites such as carbide precipitate like TiC or V_4C_3 can capture H and consequently impede its diffusion in the material (Takahashi et al. 2018), (Takahashi et al., 2010), contributing to enhanced resistance to HE. There are several types of trapping sites including diffusible traps that do not capture H, allowing it to re-enter the lattice. Sites in the materials that trap more deeply with a binding energy in the range $0.3\,eV/atom < E_b < 0.6\,eV/atom$ like vanadium carbide are considered reversible. The trap which can be considered irreversible where the binding energy is high, with $E_b > 0.6\,eV/atom$ (Pressouyre, 1979) like titanium carbide precipitate, deformed Fe_3C located at grain boundaries in steel (Song et al., 2018) or microvoids in iron (Lee et al. 1987) for example**.** Certain materials also enable the trapping and storage of a significant amount of H in a solid state, with the ability to release or unload it at a later time by increasing the pressure or temperature (Andersson et al. 2019) (Sandrock, 1999). Vanadium, niobium, titanium, carbon, magnesium, and zirconium are generally listed as favourable species with a high capacity of H storage (Chandra, 2008).

However, in the context of a better detection of H in APT, and a more precise localization and understanding of its trapping sites, several issues have been raised. First of all, H is consistently present in APT analyses, due to vacuum contamination. Even at ultra-high vacuum level (10^{-11} mbar), H can be detected in residual gas within the analysis chamber

(Felfer et al., 2022) (Sundell et al. 2013), either from vacuum contamination, or as a result of sample preparation through focused ion beam (FIB) or electropolishing (Yoo et al., 2022) (Chang et al., 2019). Predominantly present as H^+ and H_2^+ at 1 and 2 Da (McCarroll et al., 2020), (Mouton et al., 2019), H can also form hydrides depending on the considered chemical species. The presence of H^+, H_2^+, or even H_3^+ is strongly electric field related and analysis using laser mode are more detrimental to quantification of H (Breen et al., 2020). The presence of molecular H is explained by the lower electric field at the apex in laser pulsing mode resulting in less dissociation of the cationic H_2^+ molecule. For example, in atom probe analysis, aluminum tends to form hydrides, such as $AlH^+, AlH_2^+ \text{ and } AlH_3^+$ measurable at 28, 29, 30 Da , respectively, on a mass spectrum (de Geuser, 2006). This presence of H in the chamber can introduce biases in the characterization of H atoms originating from within the material itself.

Another challenge is the high diffusion coefficient of H in materials given that H is the lightest element. Therefore, it becomes necessary to cool down the tip at the lowest possible temperature to mitigate thermal diffusion. For example, in Ni, H exhibits an activation energy $Q = 0.47\,eV$ with a pre-exponential factor $D_0 = 4 \times 10^{-6}\,m^2.s^{-1}$ as determined through ab-initio computations (Wimmer et al., 2008). At room temperature T = 293K, the diffusion length path reaches several hundred of nm in seconds ($\lambda = \sqrt{2Dt} = 230\,nm$ in 1 second). Considering the sub-micron size of an APT specimen, all H atoms will diffuse out of the analyzed region in a few seconds at room temperature. Therefore, H loading requires a cryogenic transfer to atom probe which is still very cumbersome, because it requires a very good control of temperature and vacuum level during the sample transfer.

The other way to study H is a method developed by Kirchheim group's (Gemma et al. 2009 ; 2011) and reused by Takahashi in 2010 (Takahashi et al. 2010 ; 2018). It consists of loading the specimen in a cell attached to the analysis chamber. In Takahashi's setup the specimen can be heat treated at high temperature (*T > 500 K*) under low pressure (0.8 bar of H_2) to load H in the material and get a rapid diffusion (Bagot et al., 2006) (Devaraj et al., 2022). The specimen is then rapidly transferred to a cold head, to cool down the specimen as fast as possible (T= 70 K and less than 3 minutes) to then analyze it. This method was proven successful to analyze deep trapping sites in various steels but does not enable the study of diffusive H. Note that D_2 gas was used instead of H_2 to distinguish internal H to contamination in the analysis chamber (Takahashi et al. 2019). Note also several

preliminary works that have studied the in-situ implantation of H (Walck et al. 1984) or D (Kellogg et al. 1980) in W specimen. In these cases, ion implantation was done outside the analysis chamber, and suffer from the same limitations of rapid diffusion of H.

An alternative route to the direct charging of a gas inside the specimen was proposed and used by J.Y Cavaillé in 1978 (Cavaillé et al. 1978) and O.V Dudka in 2013 (Dudka et al., 2013). This method involves implanting directly into the APT analysis chamber through electronic emission with a negative constant voltage applied to the specimen. In this process, field emission from the specimen (a sharply pointed needle), is employed to ionize the surrounding H_2 gas. The produced cations are attracted by the negatively biased specimen, and can enter directly into the material, without the need of additional heating. Since cations are produced very close to the specimen surface, ions are accelerated to a low kinetic energy, typically in the range of 50 - 150 eV. O.V. Dudka estimated the implantation energy of He^+ ionized by this process to 130 eV. Sub-surface implantation has been carried out in a W sample with He^+ ions. The majority of implanted ions are estimated to reach a depth of around 1.5 - 2 nm in a FIM specimen. However, the implantation dose and the implantation depth were found limited by the maximum electronic emission possible with W. Indeed, under a negative DC electric field of $F = 8\,V.nm^{-1}$ (about 800 V on a 20 nm radius W specimen), a maximum possible electronic emission of $J = 10^{12}\,A.m^{-2}$ is reached. Beyond this value, frequent tip rupture is observed, likely induced by surface heating which is a combination of Joule heating and Nottingham effect (Paulini et al.1993). This limitation significantly restricts the achievable dose of H implantation of H using this method.

In this paper we propose an alternative way to implant directly H in metallic samples held at cryogenic temperature. To address the limitations of the maximum electric field achievable, we have developed a setup that enables in-situ ultrafast pulsed implantation (width < 2 ns) of H. Using negative pulsing implantation in a wide voltage spanning from -3,000 V to +3,000 V, we have significantly increased the maximum electric field and the achievable current from the specimen by several order of magnitudes. For example, in W case the limiting negative electric field can be more than doubled from 8 to 17 - 19 $V.nm^{-1}$. The pulsing capability avoids thermal accumulation, and overcomes shortcomings of classical gas charging and field emission implantation.

Materials and methods

Samples and preparation

The materials employed in this study are pure tungsten (W) and pure nickel (Ni) in coil form and the atom probe tomography (APT) specimens are prepared using the electropolishing process (Lefebvre-Ulrikson 2016). W is chosen for a better comparison with Dudka's work. Ni was chosen because of its high yield in APT analysis, and because like V and Ti this material has a high H solubility. It can absorb a large quantity of H (several percents) without forming brittle hydride phases (Dolan et al., 2015) (Schmidt et al., 1989). The electrolytic solution used for W is 3% NaOH in water. Solutions used for electropolishing Ni materials are firstly a solution of 90% acetic acid and 10% perchloridric acid, followed by a second step using 98% monobutyl ether and 2% perchloridric acid (Miller et al. 2014).

Instruments

Pulsed in-situ implantation was conducted on two homemade instruments; a field ion microscope (FIM) and an atom probe tomography (APT) instrument named High Resolution Tomographic Atom Probe (TAP-HR). Initially, FIM was employed to image the specimen's surface and investigate implantation defects, followed by APT to obtain atomic resolution to locate H atoms in 3D space.

The FIM setup used in this study is a 3D FIM configuration from the GPM laboratory featuring an 8 cm diameter micro channel plate (MCP) with a phosphor screen placed at a flight length L = 4 cm from the specimen. A gas ramp enables dynamic gas introduction of H_2, Ne or He gas under a maximum pressure of $\sim 10^{-5} mbar$ (Klaes et al. 2021). A DC voltage of up to 15 kV can be applied to the sample, and a cooling system achieves a minimum temperature of approx. 20 K. Voltage pulses can be applied to a counter electrode with an aperture approx. R = 1.5 mm, positioned at 0.5 mm from the sample apex. Positive or negative pulses can be applied to the counter-electrode. A voltage pulsing system with a maximum of 4,000 V was used featuring a pulse duration of about 1.5 ns, and pulse repetition rate adjustable in the range 100 Hz - 100 kHz (FPG 4-100NM1).

Additionally, a high voltage pulse inverter was employed to generate positive pulse in Figure 1a on the counter electrode (see in Figure 1b).

The atom probe (TAP-HR) setup in this paper is a homemade atom probe operating in voltage pulse mode, equipped with a large angle reflectron (Panayi et al., 2006). The setup was designed to integrate a MCP- delay line detector (DLD) detector equipped with an 8 cm DLD detection system (Da Costa et al., 2005). A schematic drawing of the setup is displayed in Figure 1c. The detector consists in of funnel-type microchannel plates with an estimated open area ratio of 90%. The total detection efficiency of the instrument is approximately 42% due to the presence of the reflectron mesh. The acquisition software and data analysis are performed using Gpm_3dSAT (Da Costa 2023) software enabling analysis at a maximum pulse repetition rate of 100 kHz , with a final maximum acquisition rate of 10^5 atoms per second. The equivalent free flight length is L = 53 cm and all analyses were done with a pulse fraction $f_p = 20\%$ with low detection rate $0.1\% < \phi < 0.3\%$ at $f = 100\ kHz$. The instrument achieves a mass resolving power of approx.1200 FWHM on a Ni^{2+} peak in pure Ni analysis. A positive voltage pulse facility from Megaimpulse with a maximum voltage of 3,000 V, pulse duration of 1.8 ns was coupled to the specimen holder (PPG-4/100). A high voltage pulse invertor with manual switch was installed to achieve negative pulsing directly on the sample.

Both instruments were modified to incorporate a pulse inverter, a gas ramp and a UHV micro-leak valve to control precisely the H_2 gas flow in analysis chamber from 10^{-10} to 10^{-4} mbar as illustrated in Figure 1b, 1c.

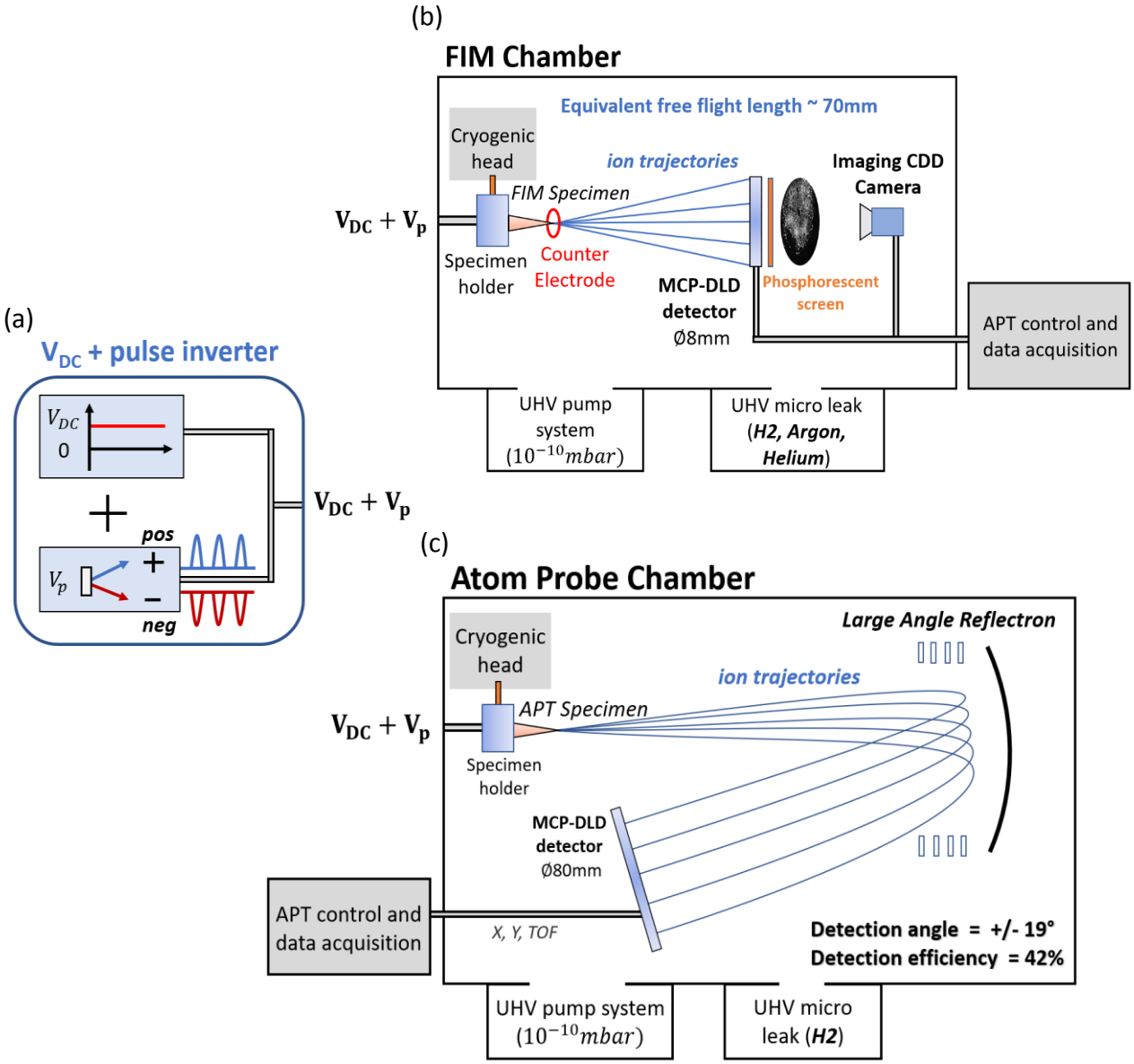

Fig. 1. *A schematic of the two home-made installations is presented with (a) the pulse inverter. (b) The FIM chamber and (c) APT chamber with both the V_{DC} and pulse inverter enabling to apply positive or negative nanosecond voltage pulse on the atom probe specimen.*

In-situ pulsed implantation simulation

Experimental results were compared to simulation performed with two software applications primarily used to model each step and compare with experimental outcomes. The first software utilized was *Lorentz-2E*. Modeling the system under the Lorentz-2E software allowed for the examination of electron emission dynamics. *Lorentz-2E* is an electrodynamic modeling software designed to calculate electric fields, currents, trajectories

of particles dynamically or statically in a modeled system. It enables the calculation of electric fields in static or quasi-static configurations (without a magnetic field). The model assumes rotational symmetry of the system, and the boundary element method used to solve the electric field problem allows for the definition of the sample geometry (with nm resolution) and the macroscopic details of the chamber (Rousseau et al., 2020), (Loi et al., 2013).

The second software employed was Stopping Range of Ions in Matter (SRIM) 2013 version (Bromley, 1985) which simulates the implantation of a particle into a target surface and its resulting effects , such as created defects, depth penetration and implantation profile. These effects depend of the nature of the particle, its impact energy and the target materials; in this case, W and Ni are the target materials. The software calculates the ion distribution depth and the occurrence of damage events. It can be noted here that SRIM simulations may exhibit some biases compared to experiments. Specifically, targets are considered amorphous, so the simulations do not take into account the crystallography, the planes orientations, and thus the possible effects of channeling that could influence the estimation of depth during implantations.

Principle and theory of in-situ implantation

Basic principles of FIM and APT

Note that under the effect of the voltage applied to the tip apex, an intense electric field (F) is generated at the apex. This field is proportional to the inverse of the radius of curvature (R) at the apex of the tip, as shown in the following equation 1 (Müller et al. 1956) :

$$F = \frac{V}{k_f R} \qquad (1)$$

k_f the field factor, is a slowly varying with R. This factor is dependent upon the geometrical electrostatic configuration, specimen shank angle and the distance from specimen to the counter electrode (Lefebvre-Ulrikson 2016) (Hyde et al., 1994) surrounding the specimen and has a value between 3 and 5 in our APT and FIM configurations. Assuming standard values of R between $20 - 100\,nm$, with $k_f = 3 - 5$ in our case due to the distance from the tip to counter electrode estimated around $500 < L < 800\,\mu m$ and due to half shank angle

around 10°, the generated electric field is about $10 - 60\, V.nm^{-1}$. This high electric field allows to evaporate and analyze a specimen tip at atomic scale.

DC in-situ implantation

DC in-situ implantation theory and limits

When a constant negative voltage is applied to an APT specimen, a negative electric field is generated at the tip. This electric field induces electron emission characterized by the density of electrons emitted in A/m² at the apex of the specimen. This density follows an exponential law known today under the name of Fowler-Nordheim (FN equation, eq. 2). Previous studies involved emitting electrons from a tip in a gaseous environment. Dudka (Dudka et al., 2013) emitted electrons into a FIM chamber where He gas was introduced. The electrons emitted from the tip ionize the surrounding gas, creating He cations. These positively polarized cations are attracted to the negatively polarized tip, re-entering the sample with a defined kinetic energy, providing implantation energy. Implantation tests in W were conducted under DC voltage application, limiting the negative voltage to -495V due to the field limit of 8 V.nm^{-1} with an electronic current density restricted to $10^{12}\, A.m^{-2}$. The primary concern is the potential fracture of the tip by thermal heating resulting from electron emission (Paulini et al. 1993). This voltage constrains the electric field and consequently the implanted dose as limiting the quantity ionized and implanted. Dudka estimates the current from the tip to be around 0.3-0.4 µA.

In this study we employed the more refined prediction of electron emission form eq. (2) (Paulini et al. 1993) based on the FN equation.

$$J(F,\phi) = \frac{q_1 F^{q_2}}{\phi^{q_3}\left(1+q_4\frac{\phi^{q_5}}{\phi^{q_3}(1+q_4\, F^{q_6})}\right)} .\ exp^{\left(q_7\frac{\phi^{q_8}}{F^{q_9}}\right)} \quad (2)$$

The flux of electron emitted J at the apex depending on the electric field and the work function of electron. For more details about constants see in Supplementary Section 1. For Ni and W, materials used in this paper, the work function is respectively $\Phi = 5\, eV$ and $4.5\, eV$ (Lefebvre-Ulrikson, 2016) (Hölzl et al. 1979).

When there is gas in the analysis chamber, this emission of electrons ionizes the environment gas inside the electronic emission cone Figure 2.

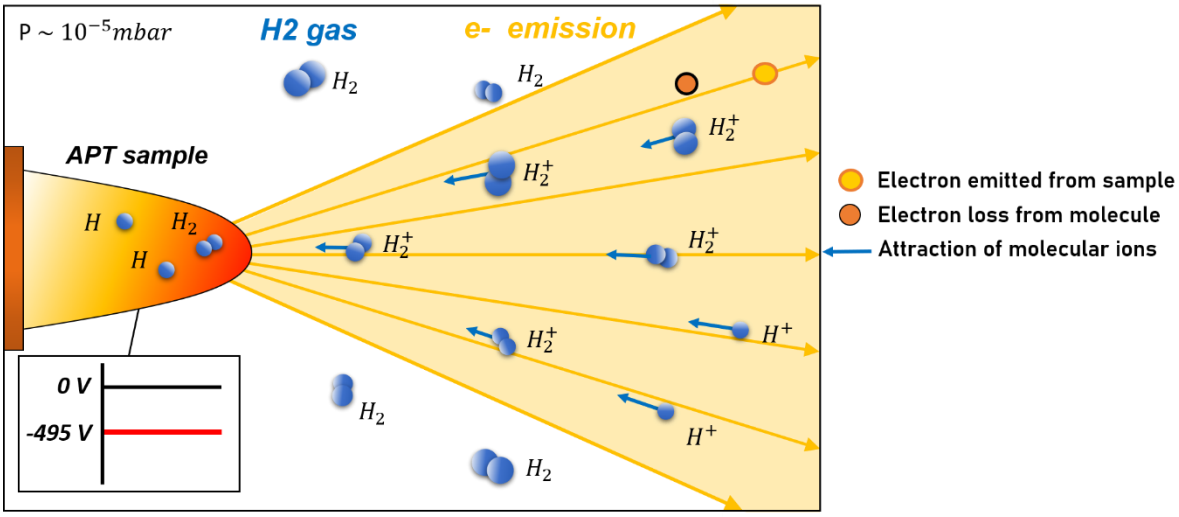

Fig. 2. *In-situ implantation of H_2 in analysis chamber in Atom Probe Tomography (APT). These molecules are ionized by the electron emitted from sample and attracted into an APT sample.*

Ionization depends on the nature of the gas and the impact energy of electrons. In this study gas in use is H_2. The quantity of ionized molecules depends on the gas pressure in the chamber and on electron kinetic energy of electrons emitted from tip. For all implantation of H, the pressure was set at $P = 5.0 \times 10^{-5}\ mbar$. Throughout the analyses, the pressure in the chamber was set at $P{\sim}10^{-10}\ mbar$. In the literature (Mazilov, 2015), (Straub et al., 1996) , the cross section of ionization between the energy of electron and H_2 gas (H^+ or H_2^+) can be obtained as shown in Figure 3. The ionization cross section between electron and H_2 gas is a function of the electron kinetic energy. The cross section is almost $10\times$ higher with H_2 than H because the H_2 occupies a larger space in Figure 3a. In Lorentz-2E simulations, the electrons kinetic energy with tip distance is available, making it possible to determine the cross section with tip distance for different electric field as illustrated in Figure 3b. It is important to note that because electrons are very fast (electrons velocity $v_e{\sim}10^7\ m.s^{-1}$) the temporal voltage variation around the specimen is negligible for electrons hitting the H_2 gas in the sub-mm region around the tip where the ionization take place. Therefore, DC calculation can be performed for electron emission.

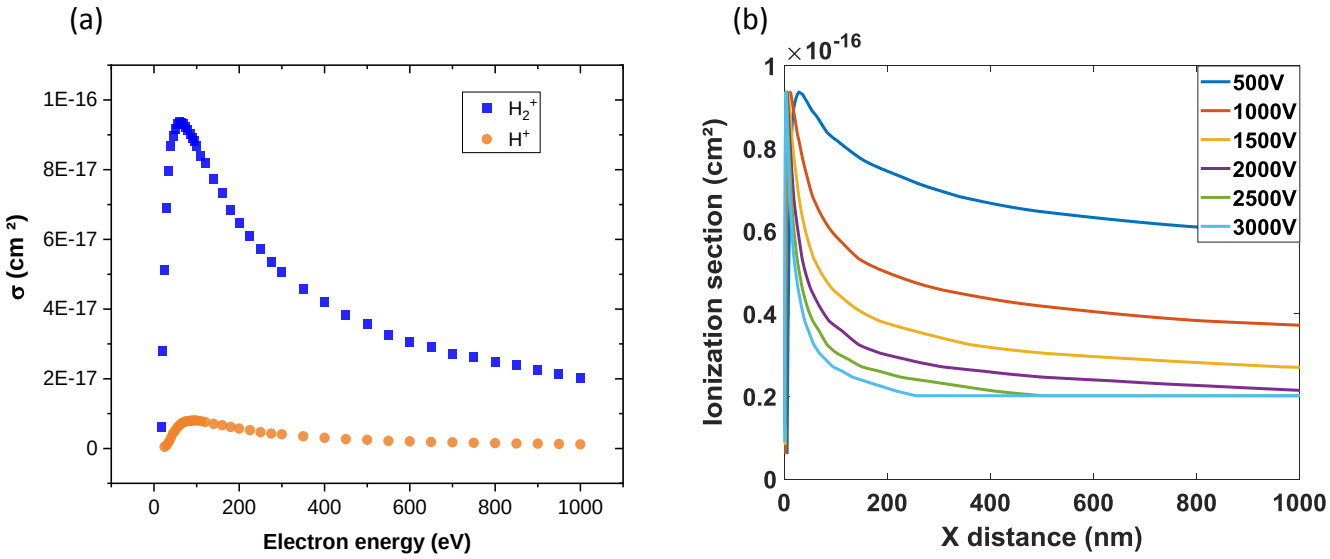

Fig. 3. *(a) H_2^+, H^+ partial cross sections with kinetic energies of electron from 10 eV to 1000 eV. (b) The influence of the cross section with tip axis called X distance on different electric field electronic emission simulated on Lorentz-2E.*

The positive ions created are attracted to the tip due to the negative bias of the sample. Since most of the ions are produced in the first micron in front of the tip, the impact of variation of the field under the application of the voltage pulse is small. Note this impact is considered in Lorentz calculation, since all the simulations were done with a quasi-transient approximation using a constant negative voltage or nanosecond negative voltage pulse. Finally, the integrated kinetic energy induced by the attraction of the ion between the initial position and the final implanted position is the energy of implantation of the ion is calculated.

Dose range and energy of continuous implantation in situ in APT

An estimation of the dose implanted in DC mode was made, considering the parameters of implantation. Mazilov (Mazilov, 2015) calculated the ions' number implanted in a standard FIM specimen for a constant electronic current. The estimated number of ions implanted during bombardment takes into account the cross section between electron and gas σ (m²), the current $I\ (A)$, the curvature radius $R\ (m)$, the pressure $P\ (Pa)$, the gas nature k_{BS} , the temperature $T\ (K)$ in equation (3) :

$$N = k_{BS}\frac{pI}{kTe}r_0\sigma(V_0) \quad (3)$$

In this study we have k_{BS} for different gases and curvature radii. Assuming a curvature radius of R = 50 nm, therefore k_{BS}= 13. Dudka et al. (Dudka et al., 2013) estimated the implanted flux to be around $1\,ions.nm^{-2}.s^{-1}$ with an average implantation energy of He^{+} around 130 eV. The implantation remains in sub-surface between 1-2 nm of depth. Mazilov (Mazilov, 2015) estimated the flux of H implanted at $15\,ions.nm^{-2}$.

Results

Pulsed in-situ implantation simulations

Emission of electrons in pulsed regime

Switching to a pulsed regime, allows electrons to be emitted at each pulse, reducing thermal stress on the specimen apex and enabling higher electric field emission without destroying the tip. The emission of electrons, ionization of the gas, and the influence of the ion implantation energy were studied based on their start distance from the specimen in pulsed regime.

In pulsed mode, the electronic emission limit for a pulse can be verified by decreasing the frequency as low as possible. These tests were done under low repetition rate operation ($f = 100\,Hz$). For Ni, the electronic emission limit is measured at an electric field $F = 10 - 11\,V.nm^{-1}$, corresponding to $\sim 10^{10}\,A.m^{-2}$ obtained with equation (2). Similar tests were performed with tungsten and the limit of the electric field for electronic emission is around $18 - 19\,V.nm^{-1}$ corresponding to $\sim 10^{12}\,A.m^{-2}$. Beyond this value, the tip has a very high risk of rupture. These tests were repeated several times and beyond this field, the tip could not be evaporated. When the electric field at the apex is set to $F = 10\,V.nm^{-1}$ for Ni specimen of radius R=50nm, and considering the surface of emission $S = \frac{(4\times\pi\times R^2)}{2} = 15{,}700\,nm^2$, the electronic current is estimated is around 20 – 80 µA. The estimated temperature increase is on the order of 200-800°C during a nanosecond. It is important to note that heating is localized in the first nm of the surface and a rapid cooling down of the tip is achieved by thermal conduction in the nanosecond range (Vurpillot et al., 2009), (Houard et al., 2011). Furthermore, the Ni melting temperature is 1450°C, ensuring the tip remains safe during the electronic emission and during the implantation.

The Lorentz-2E software enables the determination of the kinetic energies of electrons emitted from the tip when a negative pulse is applied. The software was used in *"Full impulse wave"* mode to simulate the impact of a pulse at the apex of the specimen tip, similar to a real one as seen in Figure 4a. The maximum voltage (V_P) is reached in 1.2 ns, and an exponential decay is chosen to achieve the pulse width of 1.8 ns, resulting in a time varying electric field in the specimen environment (Figure 4b). The kinetic energy of electrons is presented for three different pulse amplitudes on a tip with curvature radius R = 50 nm and half shank angle of 10° (Figure 4c). The calculations have been done in *"Quasi Transient"* mode respecting the geometry of the instrument used. The electrons acquire a very high energy when they are emitted from the tip in first nanometers of their trajectories, reaching rapidly an asymptotic kinetic energy corresponding to the potential difference between the tip and the detection system.

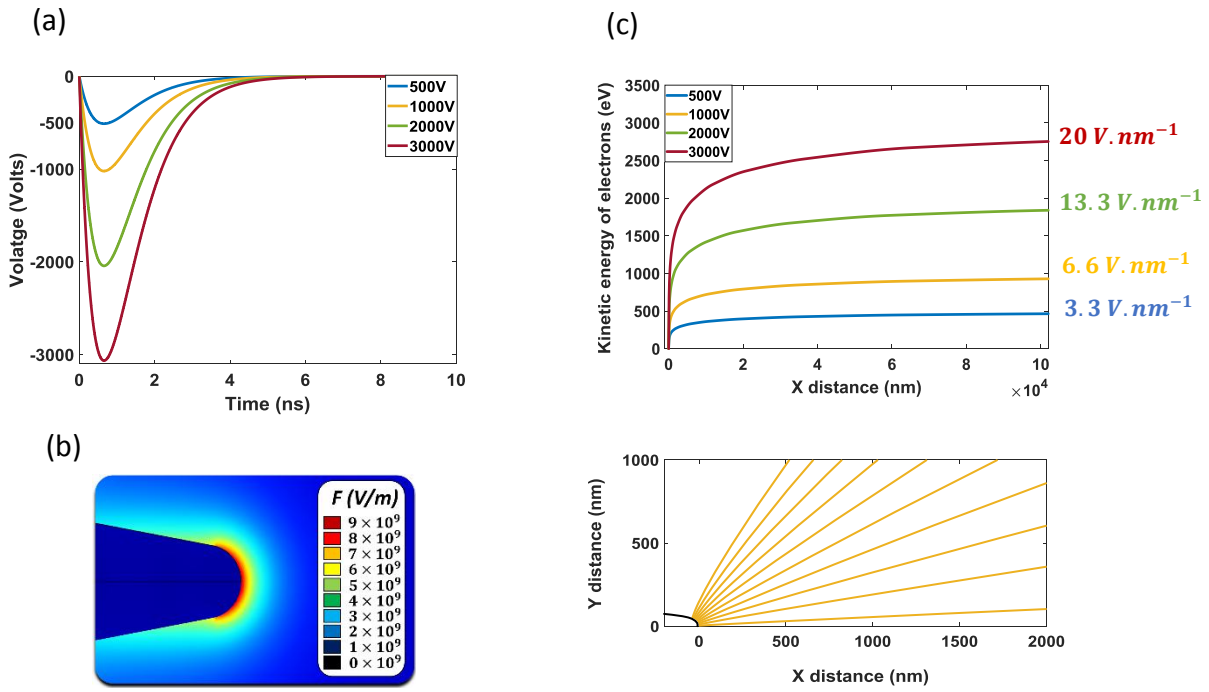

Fig. 4. *Simulation with Lorentz-2D of negative pulse using for in-situ implantation in APT. (a) Lorentz simulations are carried out with a model pulse similar to the real pulse used in APT. The rise time is 1.2 ns and the width is 1.8 ns. (b) Lorentz 2E calculates the electric field map at the apex of the tip. (c) Extraction of the data corresponding to the kinetic energy and trajectories of the electrons according to the tip distance called X distance.*

The analysis can be done in pulse amplitude ($500\ V, 1{,}000\ V, 2{,}000\ V\ and\ 3{,}000\ V$) or in electric field at the apex ($3.3, 6.6, 13.3\ and\ 20\ V.nm^{-1}$).

The various applied voltages result in differences in the acceleration phase of electrons, as depicted in Figure 4c when emitted from the tip. This difference in acceleration is reflected in the cross section as illustrated in Figure 3b. Note that electrons are extremely rapidly accelerated in free space, reaching velocity of $v_e \sim 10^7 m.s^{-1}$ in a very short time interval $\Delta t < 10^{-14} s$, and therefore results in DC mode are similar to pulse mode. In the case of a low negative voltage (-1,000 V), the lower acceleration of theses electrons results in an ionization section that extends further, as seen in Figure 3b with the red curve. On the other hand, with strong acceleration for electrons (-3,000 V), the ionization section is compressed in the first hundred nanometers along the electron's path as shown in Figure 3b (light blue curve). In all cases, a non-negligible proportion of ions remains along the electron path from 100 to 2,000 nm distance to the tip, increasing the total implantation energy which will be discussed in the next section. For example, with a field electronic emission $F = 10\ V.nm^{-1}$ on a tip with a radius of curvature $R = 50nm$ and a half shank angle $SA = 10°$ the ionization peak occurs around *5-15* nm from the tip. When the applied voltage to the sample is high, the electrons are accelerated more strongly and spatial ionization is located in a reduced region in front of the sample, as shown in Figure 3b.

In the following sections, we will study the energy of implantation of the ions when they are ionized at different distances from the tip.

In-situ pulsed implantation energy

Simulations were conducted to extract the kinetic energy values of H_2^+ ions based on their starting distance using the same Lorentz-2E setup of previous simulations. The approach involved placing several H_2^+ ions at various distances from the tip and initiating their motion when the peak of the pulse was reached corresponding to 1.2 ns (maximum of the electric pulse). Due to the negative polarization of the specimen, the positive ions are attracted to the tip. The kinetic energy of implanted ions is defined as the kinetic energy at which the ions impact the tip corresponding when tip distance equal 0 nm. As depicted in Figure 5a, the implantation kinetic energy depends on the distance at which they are ionized. Ions

ionized farther away have more time and distance to be accelerated, resulting in higher kinetic energy. Conversely, ions ionized closer to the tip have a shorter distance to be accelerated. The kinetic energy also exhibits an asymptote, corresponding to the potential difference between the voltage applied to the tip and the detector, similar to the energy of emitted electrons. It is important to note that these simulations considered the influence of the initial velocity of the molecules on their trajectory and implantation energy. The molecules in the chamber have an initial velocity *v*, estimated using the Maxwell velocity distribution law for gas (Maxwell, 1860). These initial velocities are estimated around $1{,}500 - 1{,}800\, m.s^{-1}$ with $T = 293\ K$ and $m = 2 \times 1.67 \times 10^{-27} kg$ for H_2 . However, we found that these initial velocities, have finally a negligible influence in the simulations.

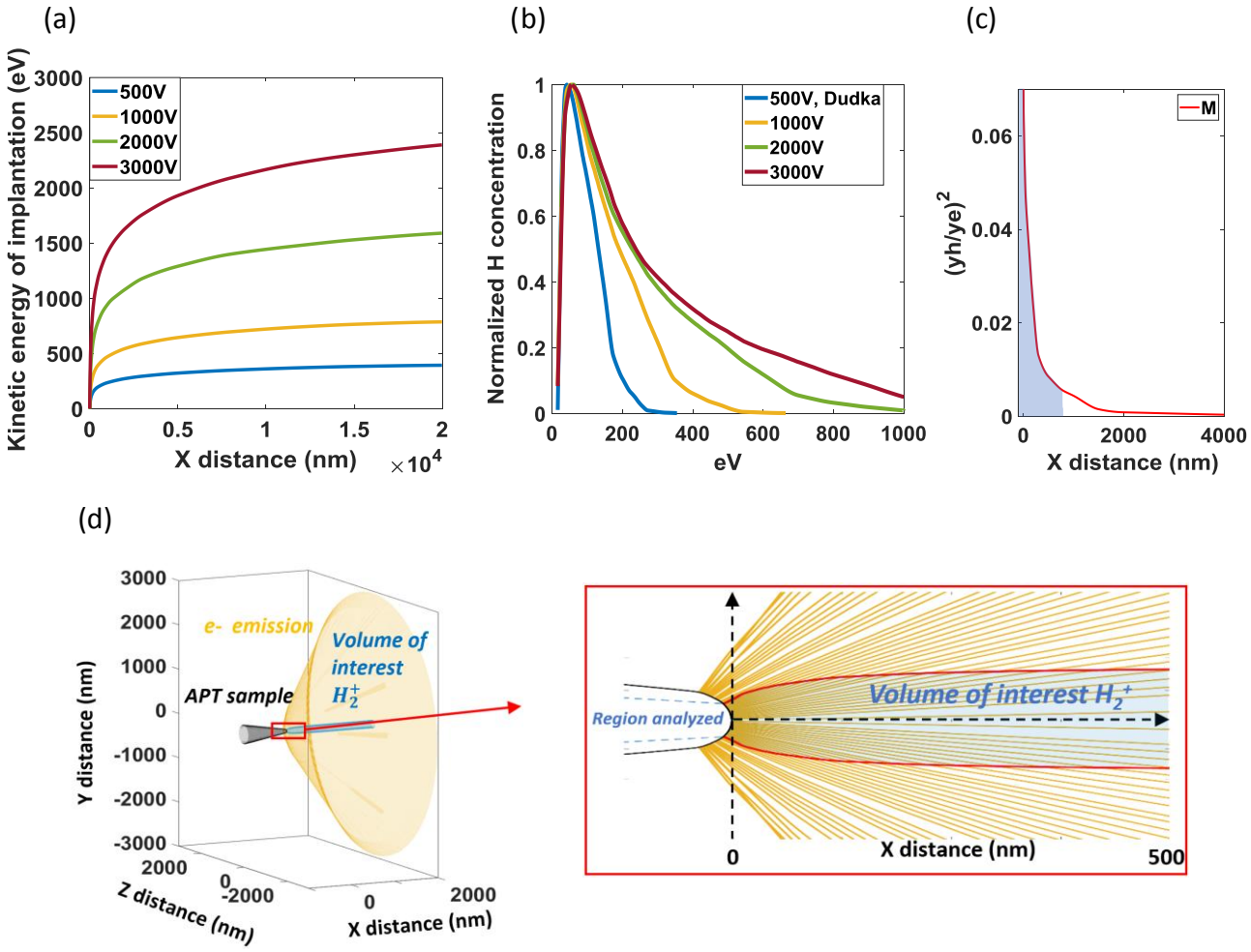

Fig. 5. *(a) Final calculated implantation energy of H_2^+ ions with distance tip for different pulses of different amplitudes. This study was done with a radius of curvature R = 50nm and a cone angle SA = 20° and $k_F = 3$. (b) Normalized number of ions implanted into the*

tip as a function of the implantation kinetic energy taking into account all physical parameters (cross section, electrons, ions and magnification in the field of view of the atom probe). (c) The magnification is obtained by dividing the cylinder disc "volume of interest" by the cone disc "e- emission". (d) The electronic cone emission in yellow curve and the volume simulated in 3D where the ions are created and implanted in field of view (FOV) of the instrument, called "Volume of interest".

Therefore, taking into account the kinetic energy of electrons in Figure 4c, the ionization cross section between electrons and H molecules in Figure 3b and the ions' kinetic energy in Figure 5a, we do a strictly interpolation between their values to determine an average implantation energy with different electric fields. The field of view of the instrument and the trajectories of the particles, described in the next paragraph, highlight that the implantation energy depends on the applied voltage. The energy at the peak of the curve in Figure 5b remains almost the same whatever the voltage (variation of less than 60 eV), primarily due to the cross section of the electrons. However, the significant difference lies in the highest energies. At -1,000 V, 20% of the implanted ions have an implantation energy of at least 200 eV, while at -3,000 V this is increased to around 700 eV.

When electrons ionize the gas with a certain energy, the ions should have the same energy in return because the potential difference between the two particles (electron/ion) remains the same. However, considering the field of view of the instrument (+/- 28.5°), a parameter called magnification (**M**) is introduced in Figure 5c and explained in the following paragraph. The effect of **M** on the implantation energy is observed because greater importance is attributed to ionization events close to the tip (distance X < 500 nm) rather than those farther away (X > 500 nm). At this low tip distance, the electrons are still in the acceleration phase and therefore their energy depends on the applied potential voltage see in Figure 5a.

The Magnification **M** has been calculated as the ratio of the surface corresponding to the ions that will be implanted in the field of view of the instrument $S_h = \pi \times y_h^2$ divided by the surface of the electron emission $S_e = \pi \times y_e^2$ with y_e the height limit of electron and y_h the ions' height limit implanted in the field of view of instrument, that was calculated along the distance to the tip in the optical axis seen in Figure 5d with volume of interest. The estimation of y_h has been done with a study of the H ions trajectory.

We can obtain the electron area density corresponding to the electron density which ionizes the gas in the field of view of instrument and it decreases drastically with tip distance, which was obtained by multiplying the number of electrons emitted from the tip Ne and M parameter. Therefore, the ions generated farther away (X > 400 nm) will be implanted on the sides of the tip.

In other words, it is essential to ionize the maximum number of molecules as close as possible to the apex. Pulsing in negative voltage allows access to higher negative voltages and electric fields of the order of 10 V.nm^{-1} on Ni, for example. This enables ionizing ions with high energy as close as possible to the specimen tip apex rather than using a constant negative voltage. The estimated average implantation energy, considering the proportions, is around 150 eV for -1,000 V, ~250 eV for -2,000 V, and ~320 eV for -3,000 V.

Depth of pulsed in-situ implantation in APT

With the simulation of atomistic collisions in a target material using SRIM, the distribution of ions in the depth of the Nickel sample can be determined. These SRIM simulations were carried out on a target with a flat surface, which obviously differs from the experiment where it involves a curved surface. We will discuss the differences this may cause in “Discussions” section. The simulations were performed with the "Detailed calculation with full damage cascade" method. The simulations are performed using 1,000,000 H ions at the maximum point where the quantity is normalized to 1. The simulations considered the proportion in energy sent without incident angle in Figure 6 for a 20 nm Ni layer with displacement energy for Nickel at *24 eV* (Lucasson et al. 1963). The work was done for negative pulses of amplitudes -500 V, -1,000 V, -2,000 V and -3,000 V.

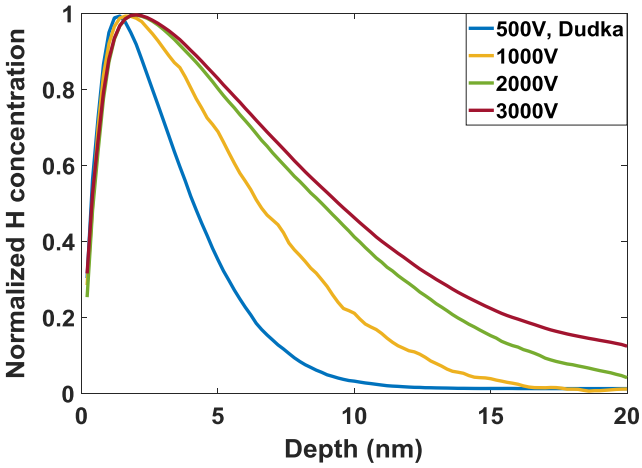

Fig. 6. *Depth implantation of H ions in Nickel simulated on SRIM considering the proportion set at intervals of 20 eV. All calculs was done with "Detailed calculation with full damage cascade" method.*

The expected depth for the majority of H ions implanted is therefore expected to be around 2-5 nm in depth in Ni and W. For -1,000 V, -2,000 V, -3,000 V the proportion of H implanted beyond 10 nm from the surface reach respectively *10%*, 15% and 25% as shown in Figure 6.

Dose range of in-situ implantation in APT

The implantation dose is strongly dependent of the global ionization rate which relies on electron emission and the quantity of H_2 molecules in the chamber. To facilitate rapid pumping of residual gas in the chamber after implantation, the pressure of H_2 was maintained at $5 \times 10^{-5} mbar$. The gas temperature matches the temperature of the vacuum chamber walls (293 K). Since the gas pressure is fixed, the electric field at the apex becomes the primary parameter controlling the final dose. In simulating the experiment, a sample with a radius of 50 nm is considered, and the voltage is adjusted to reach the chosen electric field at the specimen apex. While some variations of the electron emission and ion implantation exist with specimen shank angles, the major effect is induced by the electric field. For simplicity, the shank angle is fixed to 20°, the average value of angle for the studied specimens (samples were imaged with SEM and have an average cone angle around 20°). Note that experimentally, the electric field is known and calibrated through initial field evaporation experiments. Indeed the positive voltage is adjusted for field evaporating the pure Ni specimen ($35\ V.nm^{-1}$ according to Tsong (Tsong, 1978)).

The final quantity of implanted H in the atom probe sample in the field of view (FOV) of the instrument is governed by the following equation:

$$Dose = \int_0^X N_{ions}(x) = \int_0^X \frac{pV(x)}{kBT} \times Na \times Ne(x) \times \frac{\sigma(x)}{S_e(x)} \times \mathrm{M}(x) \times \phi_r \times dx \qquad (4)$$

Where :

- N_{ions} is the number of ions implanted in the field of view of the instrument.
- V is the volume of the electronic emission cone obtained on Lorentz-2E.
- X represents the distance along the X-axis (sampled by steps of 1nm).
- p is the pressure in front of the tip.
- Na is Avogadro's number.
- N_e is the number of emitted electrons obtained with $N_e = I \times 6.24 \times 10^{18} \times f \times t \times t_{pulse}$ where I is the current emitted from the Ni tip and depends mainly on the electric field (see in eq. 3).
- M is the magnification due to the field of view of the instrument.
- σ is the ionization cross section.
- S_e is the surface of the electronic cone volume.
- ϕ_r is the detection efficiency of the instrument (42%).

The implanted dose and density of H ions in the APT sample can be estimated using these parameters, as illustrated in Figure 7.

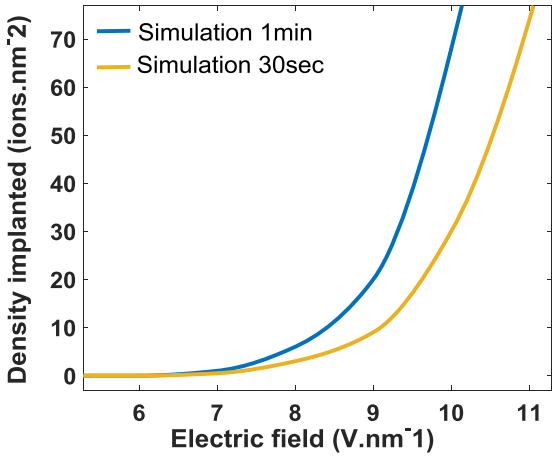

The total number of ions implanted in the APT field of view enables to calculate the density of H per nm^2 in analyzed volumes which enables to compare different specimens (with

Fig. 7. *Density per nm² of H ions implanted in-situ in APT sample with curvature radius R = 50nm, a current emitted $10^{10} Amp.m^{-2}$, a pulse frequency f = 10 kHz, during 30, 60 seconds of implantation at the apex of the tip for different electric field of implantation.*

various tip radius) with eq. (4). Note that to compare experiment to this estimation, the detection efficiency (42% in this atom probe) needs to be considered.

In-situ pulsed implantation experiments

The results presented in the next section will be organized in the following manner; first, we will report the reproduction of He in-situ implantation in FIM mode using pulse implantation compared to O.V Dudka studie (Dudka et al., 2013). In a second part, in-situ H implantation in atom probe is demonstrated in nickel samples.

Damage by in-situ implantation in Field Ion Microscopy

To validate the pulse implantation setup we reproduced the experiment of in situ implantation of He in tungsten (Dudka et al., 2013). Figure 8a shows a FIM micrograph of our W specimen just before implantation at an He pressure of 1.10^{-5} mBar. Once the DC voltage on the specimen is set back to 0 V, voltage pulses are then applied to the specimen at a repetition rate ***f*** during a time interval ***t.*** The electronic emission (FEM) can be controlled directly on the FIM screen as shown in Figure 8b. The electronic emission can be seen in this example in real time (FEM) for V_P = -1,400 V at f = 10 kHz during t = 5 minutes.

Once the implantation is done, the tip is evaporated gently with low detection rate ϕ_{det} = 0.1 - 0.2%. Detection rate values are obtained by an algorithm developed by B. Klaes called “differential method” (Klaes, 2020) (Vurpillot et al. 2023). Increasing the DC voltage (to 7,000 V), reveals the classical atomic contrast in FIM mode (Muller, 1951). By counting the successive (011) evaporated atomic terraces, we estimate the number of atomic defects produced by the implantation as a function of the depth (Dagan et al., 2017).

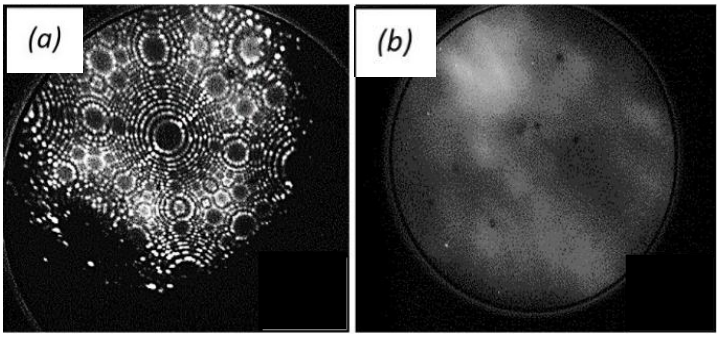

Fig. 8. *(a) FIM image of tungsten tip 011 before implantation. V_{DC}= 6,800 V, P_{HE} =1.10^{-5}mBar. (b) Pulsed FEM image of the same specimen (V_{DC}=0 V, V_p= -1,400 V, f=10 kHz).*

The consequence of He implantation at V_p= -1,400 V is clearly observed in Figure 9. Presence of numerous defects perturbates strongly the well-defined atomic structure of the tungsten surface shown in Figure 9a. These defects may be self-interstitials characterized by very bright spots, generally larger than the atoms situated on their own site. These interstitials are observed between terraces and are protruding, i.e. they will tend to evaporate first (some example in red area). Vacancies are characterized by localized dark spots (example in blue area). By gently evaporating the surface ϕ_{det} = 0.1 - 0.2%, the quantity of defects is observed to gradually decrease. Figure 9b shows the atomic surface after the evaporation of 10 (011) atomic layers (which represents a depth of 2.23 nm). The created defects in Figure 9b are then almost invisible. This indicates the implantation was efficient only on the subsurface of the sample with a low energy of implantation.

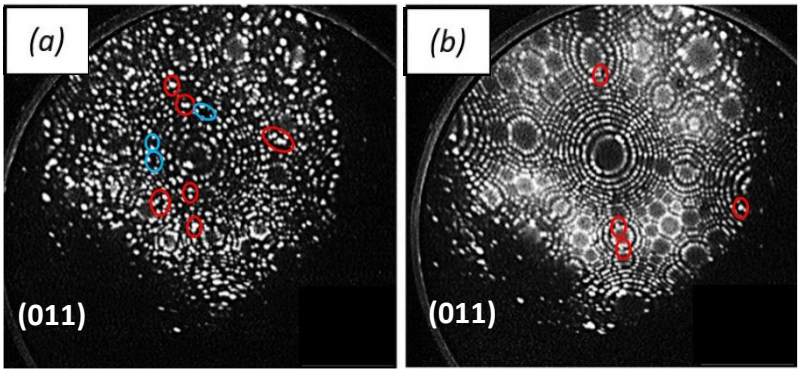

Fig. 9. *FIM images of the tungsten specimen (a) just after He implantation and (b) after the evaporation of 10 (011) atomic layers (b).*

Note that with this pulse implantation setup, it was possible to increase significantly the dose of implantation as well as the energy of implantation by raising the pulse amplitude V_p. Two tests were done at V_p = -2,000 V and V_p = -2,200 V without any fracture of the sample. More details are presented in Supplementary Section 2.

The same process was done to perform H implantation with tungsten specimens. The He gas was replaced by H_2 (P = 1.10^{-5} mBar). FIM images were performed after implantation by removing H_2 and inserting He at P = 1.10^{-5} mBar in the chamber.

The images shown in Figure 10 represent the FIM image of the tungsten surface after H implantation in the tungsten specimen with V_P = -2,500 V. As shown in Figure 10a, the FIM image of the tungsten surface implanted with H is strongly degraded by the implantation process. Note that the DC voltage is similar to the voltage before implantation. We have noticed the presence of very strong emissive spots and presence of numerous defects and roughness at the specimen surface. Conversely to He implantation, after the evaporation of 10 (011) layers (~ 2.23 nm) Figure 10b, we have noted the residual presence of atomic defects such as interstitial groups (green area) and nano-cavities (yellow area). These nanocavities generates distortions of the image due to the strong perturbation of the electrostatic surface. The created defects are bigger and deeper with the applied pulse amplitude. In the case of Figure 10c, after 36 evaporated layers (~ 8 nm), interstitial groups and cavities are still present. Application of strong negative voltage pulse (V_p = -2,500 V) leads to generation of numerous vacancy clusters and interstitials groups up to 10 nm inside the tungsten surface, much deeper than implanting He in DC mode (Dudka et al., 2013) without destroying the specimen.

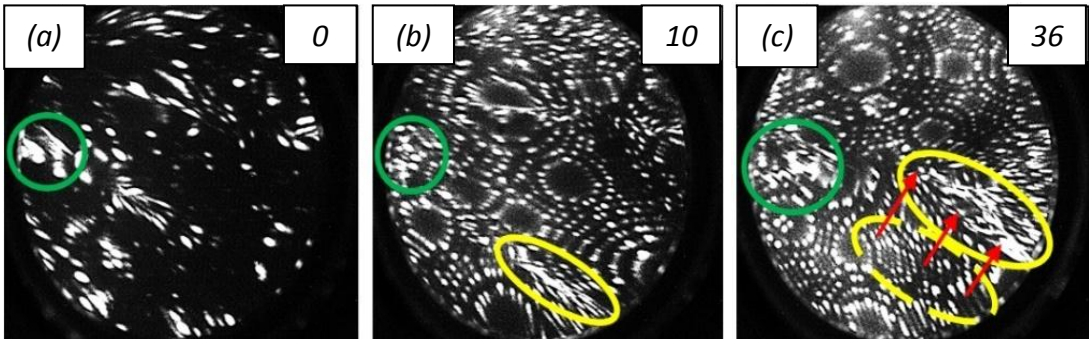

Fig. 10. *FIM images of tungsten surface after in-situ H implantation. Application of a negative pulse of V_p = -2,500 V at 10 kHz for 5 minutes. (a) Post implantation tungsten surface. (b) After 10 evaporated layers (~2.23 nm) and (c) after 36 evaporated layers (~8.0nm).*

In-situ pulsed implantation in APT

The protocol for in-situ implantation used in FIM was adapted to our APT instrument. Note that we focused our experiments on Ni, since W has a high evaporation field compared to H atoms which makes it difficult to find good analysis conditions to perform quantitative APT measurement of H. For implantation in Ni specimen, we also limited the maximum pulsed

electric field to avoid specimen rupture. Several tests were done on Ni specimen raising progressively the amplitude of negative pulses. An empirical electric field limit at 11 V.nm^{-1} was found (-11 V.nm^{-1}). Above this value, the probability of specimen rupture was found very high. The specimen is first analyzed in APT and a thin layer of material is removed from the apex (~100,000 atoms). This first step is extremely important to have a smooth and regular tip surface, since the electronic emission is very sensitive to the field. The voltage used to reach the evaporation field is used to evaluate the k_F factor assuming an evaporation field of 35 V.nm^{-1}. The DC voltage is then set to zero. A residual pressure of 10^{-5} mbar of H_2 is inserted in the chamber, and negative pulses (amplitude V_p, pulse repetition rate f, applied duration t) are applied to the specimen. After implantation, the H_2 leak valve is closed to go back to a clean ultra high vacuum level (~ 10^{-10} mbar after a few hours). Note that we maintain the tip at the lowest temperature (~20 K) during this stage. Once all these steps have been completed, the sample can be analyzed with implanted H being measured in the depth of the sample. APT analyses were obtained for different conditions of implantation on different tips. These implantation tests here were done in pure Ni samples. Figure 11 presents a successful APT analysis of a typical in-situ implantation of H in Ni. The tip presents a major direction <111> close to the tip axis (Ni specimen are wires with preferential <111> crystallographic orientation). A clear implantation of H is revealed after 3D reconstruction. In this volume the maximum peak of H composition reaches 50 % at 3 - 4 nm below the tip surface.

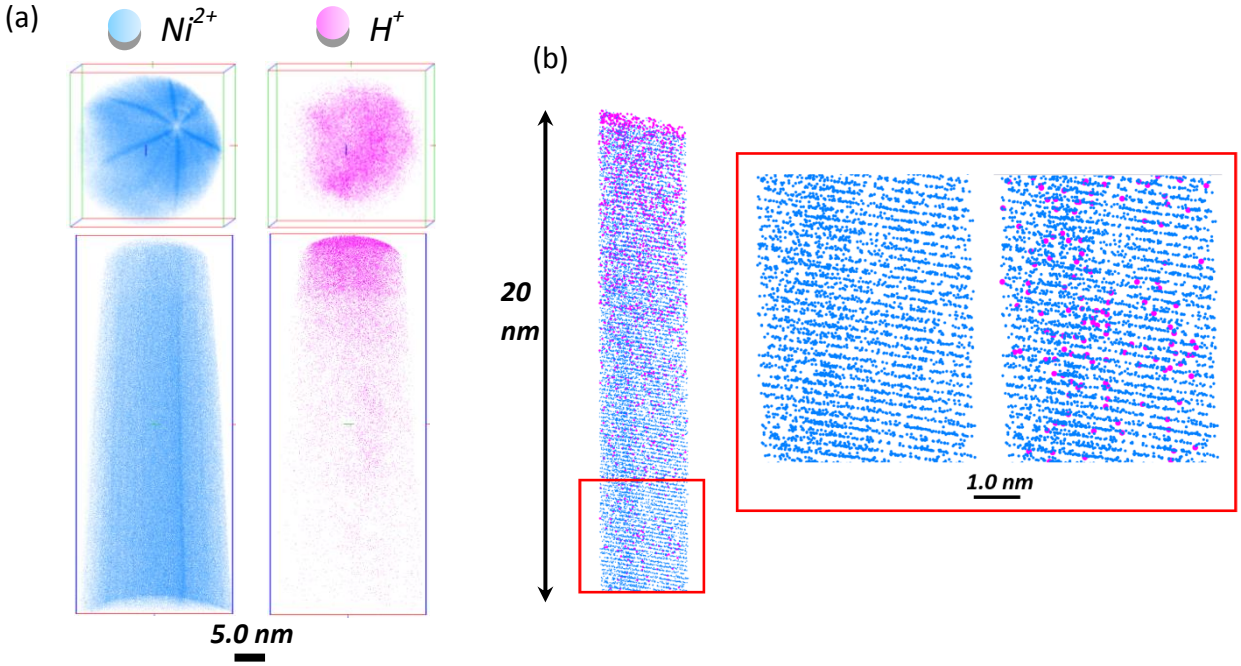

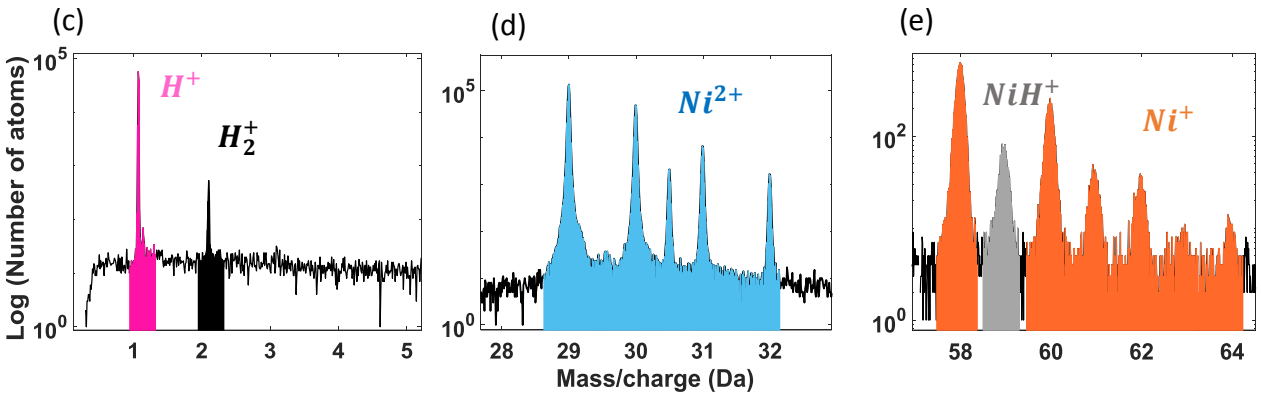

Fig. 11. *APT image of a Nickel tip with <111> crystallographic direction after in-situ H-implantation. Application of 1,000 V negative pulse at 10 kHz during 30 seconds with a gas pressure* $3 \times 10^{-5} mbar$ *in analysis chamber. (a) 3D reconstruction of the analyzed volume with Ni in blue and H in pink. (b) Zoom on the <111> reconstructed atomic planes in the first 20 nm of the volume. (c) Mass spectrum in range of* H^+ *and* H_2^+ *ions (d) in range of* Ni^{2+} *and (e) in range of* Ni^+.

We can see the implantation of H ions with the spatial localization in Figure 11a. The quality of the implantation and the spatial resolution is controlled with the presence of well-defined Ni <111> atomic planes all along the analysis in Figure 11b, the reconstruction parameters have been adjusted with the interatomic distance on the Nickel direction <111>, d_{111} = *0.203 nm* (Fajardo, 2016). Well defined atomic planes are reconstructed after evaporation of 1 - 2 nm of the specimen surface. It may be pointed out that some implantation amorphized the tip in this sub-surface region and the crystallography of the sample was partially or totally degraded, but in less than 2 nm of depth the atomic planes were fully resolved.

We show that the overwhelming majority of implanted ions are present as H^+ rather than H_2^+ in the sample while the majority of created ions are H_2^+ molecules in Figure 11a and Figure 11c. It can be assumed that implanted molecules can rapidly dissociate at the primary knocked off atom because the impact energy is well superior to the binding energy of H_2 molecules (~ $4.5\, eV$) (Blanksby et al. 2003). We notice a small peak at 29.5 Da (cf. Figure 11d) characteristic of a Ni hydride NiH^{2+} which is not visible in the case of a

classical evaporation. Nickel hydrides at 59, 61, 62, 63, 64 Da often appear after H implantation as shown in Figure 11e. We also have the presence of a hydride at 59 Da. In addition, natural abundances of N_i^+ are not respected, especially on the peak at 61 Da which should normally have a natural abundance of 1.14% and at 62 Da a natural abundance of 3.63% which is clearly not the case here with an approximate abundance of 5.20% and 4.12% respectively.

To verify the nature of the implanted profile, note that we tested also specimen with no H_2 gas inside the chamber during the electron emission (~10^{-10} mbar) and specimen submitted to 10^{-5} mbar of H_2 without applying electron emission. In both cases, no implantation profile was measured. In these cases, the H amount decreases strongly with depth in the first nm of analysis reaching a constant low value identical to the contamination signal ($< 2 - 5\%$ of concentration).

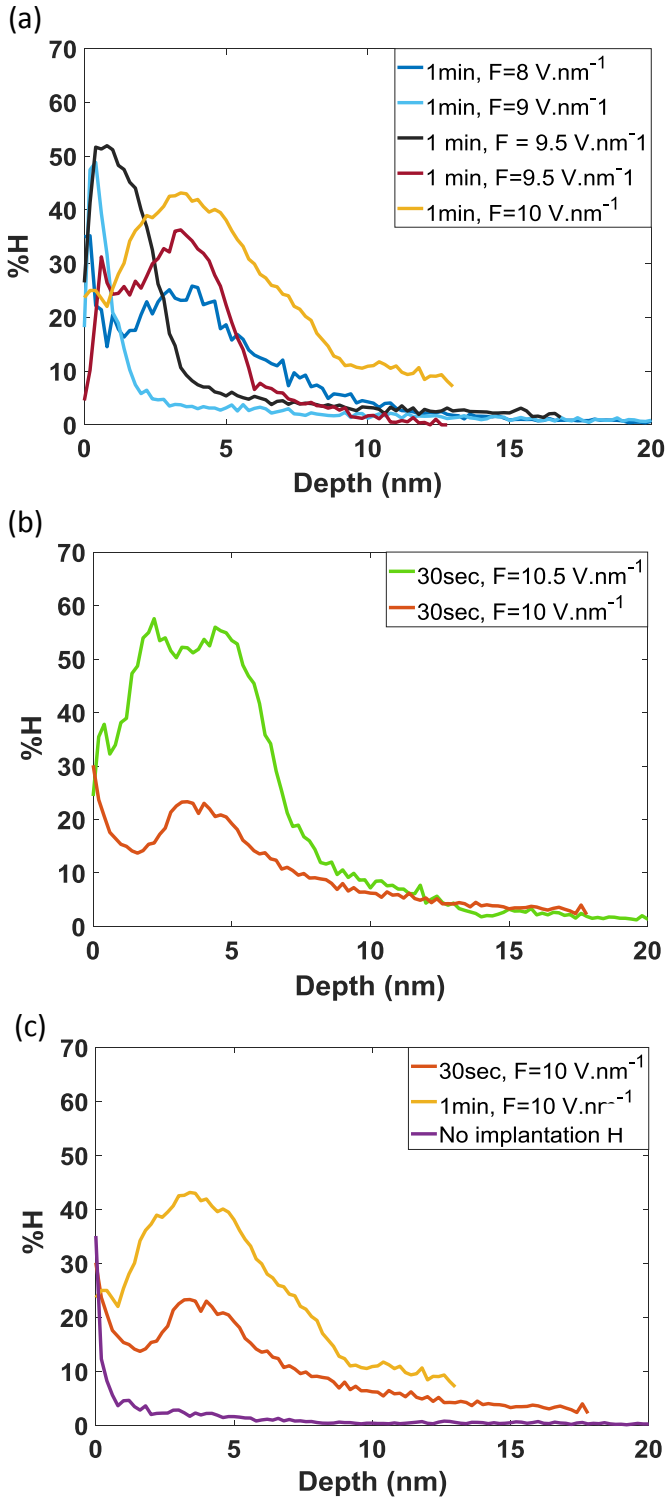

Fig. 12. *Composition profile of H^+ ions in APT analysis of Ni with in-situ implantation of H_2. These implantations were made with different negative voltage and for different times. An estimation of their implantation electric field and their density in each case was made. (a) All data experiments have been done with 1 minute of implantation for different electric field. (b) Implantation done for 30 seconds with a variable electric field and (c) shows the time comparison on the same APT sample. Theses implantations were all done with the*

same pulse frequency f=10 kHz and same gas pressure ranges 5×10^{-5}*mbar. For blue curve* $\phi_H = 20\ ions.nm^{-2}$, *dark blue curve* $\phi_H = 11\ ions.nm^{-2}$, *light blue* $\phi_H = 20\ ions.nm^{-2}$, *black* $\phi_H = 45\ ions.nm^{-2}$, *purple* $\phi_H = 62\ ions.nm^{-2}$, *yellow* $\phi_H = 54\ ions.nm^{-2}$, *green* $\phi_H = 60\ ions.nm^{-2}$, *orange* $\phi_H = 34\ ions.nm^{-2}$.

In Figure 12 APT data illustrating different profiles of in-situ implantation in the APT sample are presented. The implantation profile can vary slightly between experiment, with an earlier rising front like the light blue curve or a steeper falling front like the purple curve in Figure 12a. However, the majority of profiles share a common characteristic: most implanted ions are generally found at a depth of approximately 4 nm in the sample. Some experiments, like the light blue curve, deviate from the expected profiles, possibly due to the shape of the tip or surface roughness. Notably, the mean implantation depth remains consistent at around 4 nm, even with an increase in the electric field during implantation. These results will be further discussed and compared to the theoretical expectations in the subsequent discussion section.

A clear correlation of the implanted dose with the applied negative electric field is found, when electric field is increased, the electron emission increases exponentially and therefore the amount of gas molecules that will be ionized and implanted increases shown in Figure 12b.

Concerning the influence of the implantation time, we compare the last two experiments which were done on the same tip Figure 12c. For 30 seconds of implantation 31,500 H atoms implanted measured whereas when the implantation time is 1 minute, the number of H atoms increases to 103,000. For the first implantation the tip had an evaporation voltage of 6,250 V whereas for the second implantation the tip had an evaporation voltage of 6,450 V. This difference in voltage to be evaporated indicates a larger tip and therefore a larger emission and implantation surface. The dose is almost doubled. We can compare also the green and yellow curves which have approximately the same density of implantation, in one case 27,000 at H and in the other 103,000 H atoms. This difference is due to the size of the tip. The evaporation voltage was in the first case around 3,100 V and in the second 6,450 V. Therefore, in second case we estimate the tip with curvature radius 2X larger, so surface 4X larger. This corresponds approximately to the number of ions implanted multiplied by 4.

Discussions

The dose/density prediction of hydrogen implanted in APT sample

The dose implanted in the sample is estimated using (eq. 4) and its expected quantity is predicted. It's important to note that this quantity also depends on the tip shape. Therefore, in the subsequent discussion, the term "density dose" will be employed, representing the quantity implanted and analyzed divided by the analyzed surface. Density dose is expressed in ions per square nanometer ($ions.nm^{-2}$).

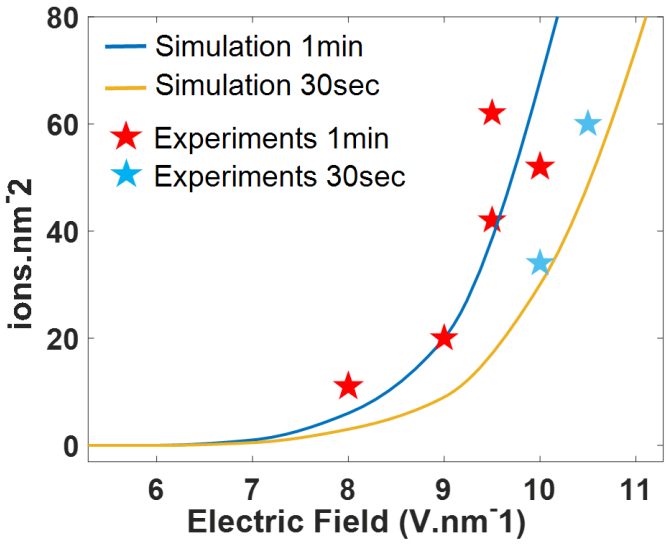

Fig. 13. *Density per nm² of H ions implanted in-situ in Ni APT sample, during 30 seconds and 1 min for different electric field of implantation with simulations and experiments comparison, each point is an individual experiment.*

As shown in Figure 13 there is a good agreement between experiments and simulations. The trend towards an exponential implantation density depending on the field is highlighted here. This trend is also apparent for different implantation times. Experiments with 1 minute of implantation have always a higher density of H ions implanted than 30 seconds for the same electric field implantation. We note that above $60\ ions.nm^{-2}$, the risk of sample rupture become considerable due to a significant concentration of H in the matrix, potentially leading to decohesion within the sample as observed in FIM experiments.

Additionally, the majority of the ions created are finally implanted on the sides of the sample shown in Figure 5c. The APT volume represents a small volume of the specimen and H collected are a small amount of the total implanted H.

Implantation profile

We can also compare theory and experiment on implantation profiles in APT sample.

In Figure 14 we have two implantations on a Ni sample at same electric field implantation (V_p = -2,200 V and -2,100 V at 10 kHz for 1 minute and 30 seconds respectively).

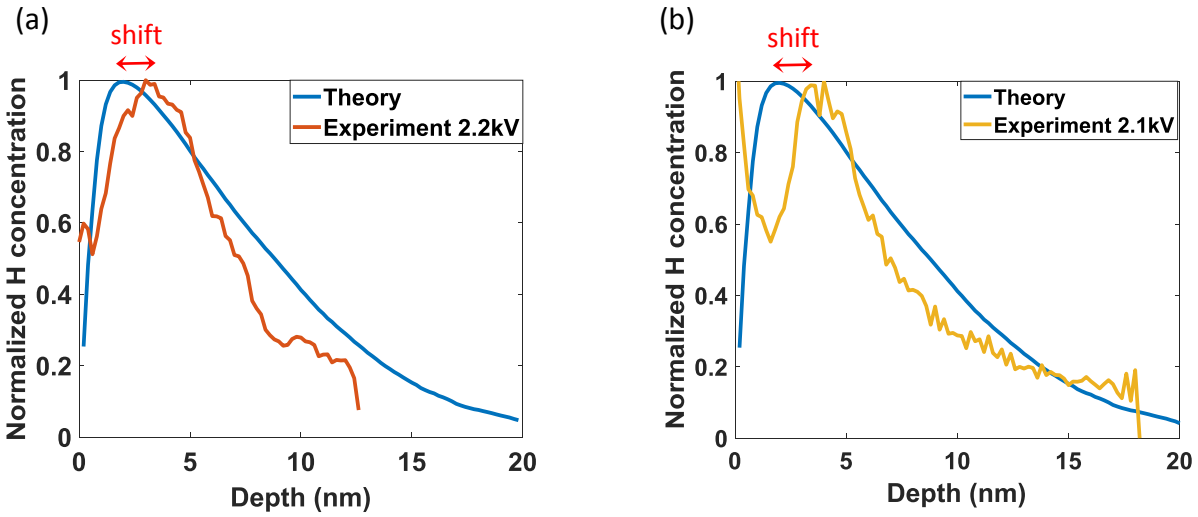

Fig. 14. *Comparison between theory and experiment of implantation profile of H in APT sample in two cases at 10 kHz. (a) -2,200 V applied on the tip during 1 minute, (b) -2,100 V applied on the tip during 30 seconds.*

The implantation profile experiments are close to the theoretical expectation, indicating a reasonable agreement between the model used for estimating the implantation energy and the experiments. It is noteworthy that peak of the implantation profile consistently appears shifted towards greater depths in experiments compared to the theoretical predictions (shift shown in Figure 14). In both cases; we observe that the experimental peak tends to be situated around ~5 nm in depth, while SRIM model suggest a maximum at 2 - 3 nm. This discrepancy can be attributed to two factors.

Firstly, the depth estimation is performed on SRIM using a flat target model, whereas the experimental implanted surface here is curved. Therefore, estimation of depth may contain a systematic bias at the top of profile. Secondly, H atoms implanted very close to the surface (subsurface) probably diffuse during the implantation and leave the surface (outgasing), that could be explain this slight deficit in the first 2 nanometers in experiments compared to the theory. It can be noted that there is a potential channeling effect that can influence both the depth and the expected implanted hydrogen density within the sample. However, this effect may be considered negligible due to the implantation trajectories of ions having multiple angles of implantation, as shown further in Figure 16 and in Figure 19 in S3, which significantly limits this channeling effect observed in the literature (Hachet et al., 2020) (Besenbacher et al., 1984) (Besenbacher et al., 1982). Simulations show hydrogen particles follow field lines and are thus implanted at various angles ranging from 0° to 45° relative to the normal of the tip as we see in S3.

Inhomogeneity of spatial implantation in APT specimen

We also note a spatial inhomogeneity of H implanted in experiments. The implantation appears dense in the core of the sample in the first few nanometers (depth < 4nm). Subsequently, this density disperses towards the side of the sample at greater depths, as illustrated in Figure 15.

Fig. 15 Density map H^+ ions' after a typical H in-situ implantation into an APT

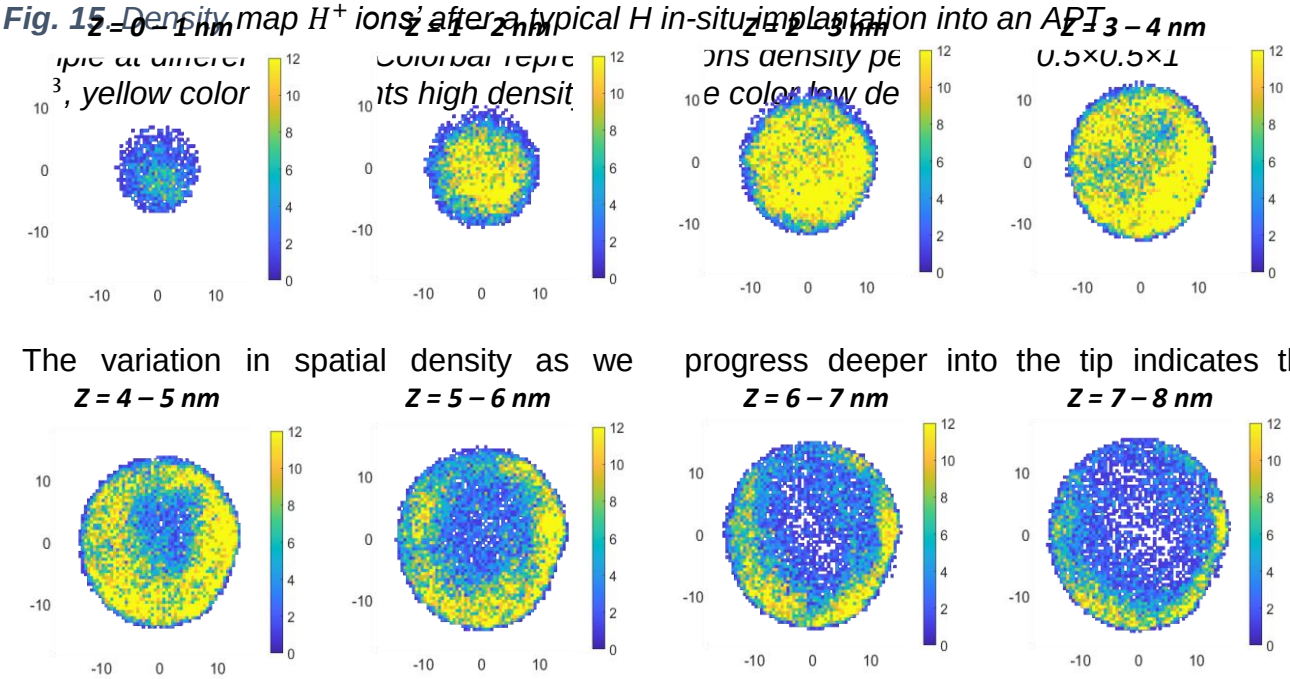

The variation in spatial density as we progress deeper into the tip indicates the

presence of two distinct types of implantations. A core implantation is observed up to depth of 4nm, while a lateral implantation occurs between 5 and 10 nm of depth. The H ions created farther from the tip apex exhibit higher kinetic energy of implantation, as illustrated in Figure 5a, and are consequently implanted at greater depths. However, the majority of ions that are created far away from the tip are implanted on the sides of the sample due to its curved surface (Figure 5b, 5c), which explains why at analysis depths greater than 4 nm the highest density of H^+ions form a crown inside the specimen around apex (shown in Figure 15 in yellow), this observation may elucidate why ions deeply implanted tend to be situated on the sides of the specimen.

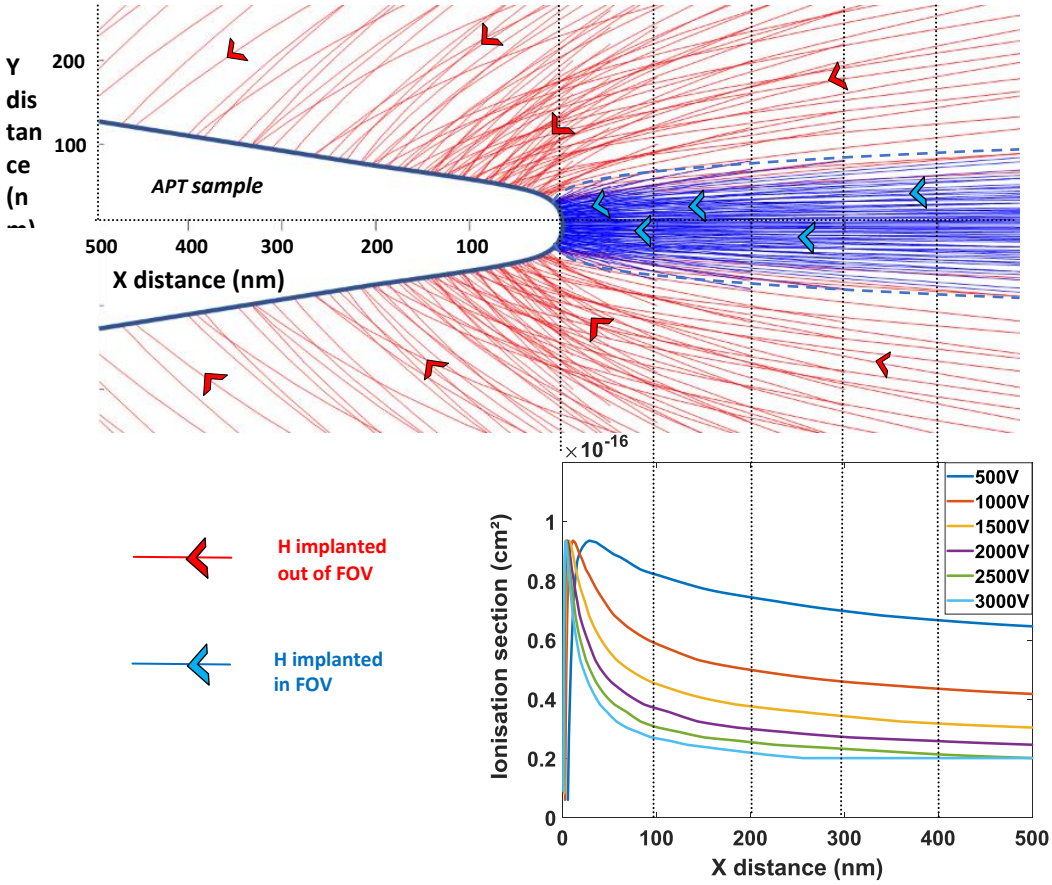

Fig. 16. *Simulations of ion trajectories implanted in two cases. First, ions generated by electron bombardment created at short distances to the apex of the sample (0 nm < X < 1000 nm) and implanted in the FOV of the APT instrument (blue trajectory). Second, ions created far away from the sample (1000 nm < X < 30 μm) implanted out of FOV instrument (red trajectory). Note the density of red ions trajectories on the edges of the specimen due to the electric field. Ionization cross-section of electrons with H_2 gas for different pulse amplitudes correlated ranging from 0 to 500 nm in front of the APT sample.*

This behavior was simulated in Figure 16 where ions implanted on the sides are those created far away to the sample and the ions implanted in the FOV are those created very close to the surface (cf. Figure 5b). The ions created far away from the sample are implanted completely outside of the field of view (red trajectory) contrary to the ions created close to the specimen's axis (blue trajectory).

Therefore, the highest quantity of ions implanted throughout the entire sample are those located beyond the field of view of the instrument. The implanted ions in the specified APT volume of interest constitutes less than 10% of the total volume of ions generated in front of the sample. As a result, the estimated quantity of ions implanted outside the field of view is approximately in the range of $10^6 - 10^7\ atoms$.

Therefore, the main interest is to have the highest possible negative voltage without damaging the tip to ionize the majority of the ions very close to the surface. That allows us to reduce the issues from the trajectories and field of view and thus obtain a larger quantity of ions implanted in field of view of the instrument.

Conclusion

We present in this paper a successful method for implanting a high dose of H within the first 20 nm of a metallic sample. The objective is to investigate the diffusive trapping of H in various alloys, thereby enhancing our understanding of H behavior in materials. In-situ pulsed implantation enables us to implant a higher dose and energy of implantation compare to continuous mode. The method is simple and straightforward, the theory and the experimental are consistent, but good control of many parameters is required. These parameters relate to the implantation and the instrument of course but also related to the tip shape. The implantation profiles are satisfactory, the implantation of H ions in Nickel reaches a depth of 4 nm with a significant quantity collected in a standard APT volume (*~100,000 atoms measured*) with up to *10%* remaining at *10 nm* of depth. Pulsed implantation allows to reach a higher negative voltage amplitude compared to constant voltage, facilitating the ionization of a larger quantity of ions close to the apex and, consequently, thus to implant a large quantity in an atom probe specimen with moderate kinetic energy (~1000 eV).

This in-situ implantation approach makes it possible to avoid the cumbersome cryogenic specimen preparation protocol, as implantation occurs directly in the analysis chamber of the atom probe instrument at very low temperatures ($20\ K < T < 80\ K$). This enables a study of H in materials with a relatively good statistical accuracy and predictability. Consequently, this method appears today as a good alternative for studying H in materials at the atomic scale. In future studies we will test this method on other materials like pure Fe, Sc, Zr and Ni-Mo, with a further aim of also studying the temporal nature of different trap sites including microstructural features such as grain boundaries and dislocations. This method can be employed as H charging to observe trap site in materials and study the spatial distribution of H in APT specimens.

References

Andersson J & Grönkvist S (2019). Large-Scale Storage of Hydrogen. *International Journal of Hydrogen Energy* 44 (23): 11901‑ 19. https://doi.org/10.1016/j.ijhydene.2019.03.063.

BAGOT, P. A. J., VISART DE BOCARME, T., CEREZO, A. & SMITH, G. D. W. (2006). 3D atom probe study of gas adsorption and reaction on alloy catalyst surfaces I: Instrumentation. *Surface Science* **600**, 3028–3035.

Barrera O, Bombac D, Chen Y , Daff T. D, Galindo-Nava E, Gong P & Haley D (2018). Understanding and Mitigating Hydrogen Embrittlement of Steels: A Review of Experimental, Modelling and Design Progress from Atomistic to Continuum. *Journal of Materials Science* 53 (9): 6251‑ 90. https://doi.org/10.1007/s10853-017-1978-5.

BESENBACHER, F., BOGH, H., PISAREV, A. A., PUSKA, M. J., HOLLOWAY, S. & NØRSKOV, J. K. (1984). Interaction of deuterium with lattice defects in nickel. *Nuclear Instruments and Methods in Physics Research Section B: Beam Interactions with Materials and Atoms* **4**, 374–387.

BESENBACHER, F., BO/TTIGER, J. & MYERS, S. M. (1982). Defect trapping of ion-implanted deuterium in nickel. *Journal of Applied Physics* **53**, 3536–3546.

Bhadeshia, H.K.D.H (2016). Prevention of Hydrogen Embrittlement in Steels. *ISIJ International* 56 (1): 24‑ 36. https://doi.org/10.2355/isijinternational.ISIJINT-2015-430.

Blanksby S.J & Barney Ellison G (2003). Bond Dissociation Energies of Organic Molecules. *Accounts of Chemical Research* 36 (4): 255‑ 63. https://doi.org/10.1021/ar020230d.

Breen, A. J, Stephenson L.T, Sun B, Li Y, Kasian O, Raabe D, Herbig M & Gault B (2020). Solute Hydrogen and Deuterium Observed at the near Atomic Scale in High-Strength Steel. *Acta Materialia* 188 (avril): 108‑ 20. https://doi.org/10.1016/j.actamat.2020.02.004.

BROMLEY, D. A. (ed.) (1985). *Treatise on Heavy-Ion Science*. Boston, MA: Springer US http://link.springer.com/10.1007/978-1-4615-8103-1 (Accessed February 6, 2023).

Cavaillé J.Y & Drechsler M (1978). Surface Self-Diffusion by Ion Impact. *Surface Science* 75 (2): 342‑ 54. https://doi.org/10.1016/0039-6028(78)90256-X.

Chandra D (2008). Intermetallics for Hydrogen Storage. In *Solid-State Hydrogen Storage*, 315‑ 56. Elsevier. https://doi.org/10.1533/9781845694944.4.315.

CHANG, Y., LU, W., GUÉNOLÉ, J., STEPHENSON, L. T., SZCZPANIAK, A., KONTIS, P., ACKERMAN, A. K., DEAR, F. F., MOUTON, I., ZHONG, X., ZHANG, S., DYE, D., LIEBSCHER, C. H., PONGE, D., KORTE-KERZEL, S., RAABE, D. & GAULT, B. (2019). Ti and its alloys as examples of cryogenic focused ion beam milling of environmentally-sensitive materials. *Nature Communications* **10**, 942.

Chen Y.S, Lu H, Liang J, Rosenthal A, Liu H, Sneddon G, McCarroll I, Zhao Z, Li W, Guo A & Cairney J.M (2020). Observation of Hydrogen Trapping at Dislocations, Grain Boundaries, and Precipitates. *Science* 367 (6474): 171‑ 75. https://doi.org/10.1126/science.aaz0122.

Da Costa G (2023). Gpm_3dSAT software. IDDN.FR.001.430017.000.S.P.2020.000.10000.

Da Costa G, Vurpillot F, Bostel A, Bouet M & Deconihout B (2005). Design of a Delay-Line Position-Sensitive Detector with Improved Performance. *Review of Scientific Instruments* 76 (1): 013304. https://doi.org/10.1063/1.1829975.

Dagan M, Gault B, Smith G.D.W, Bagot P.A.J & Moody M. P (2017). Automated Atom-By-Atom Three-Dimensional (3D) Reconstruction of Field Ion Microscopy Data. *Microscopy and Microanalysis* 23 (2): 255‑ 68. https://doi.org/10.1017/S1431927617000277.

DEVARAJ, A., BARTON, D. J., LI, C., LAMBEETS, S. V., LIU, T., BATTU, A., VAITHIYALINGAM, S., THEVUTHASAN, S., YANG, F., GUO, J., LI, T., REN, Y., KOVARIK, L., PEREA, D. E. & SUSHKO, M. L. (2022). Visualizing the Nanoscale Oxygen and Cation Transport Mechanisms during the Early Stages of Oxidation of Fe–Cr–Ni Alloy Using In Situ Atom Probe Tomography. *Advanced Materials Interfaces* **9**, 2200134.

Dolan M.D, Kochanek M.A, Munnings C.N, McLennan K.G & Viano D. M (2015). Hydride Phase Equilibria in V–Ti–Ni Alloy Membranes. *Journal of Alloys and Compounds* 622 (février): 276‑ 81. https://doi.org/10.1016/j.jallcom.2014.10.081.

Dudka O. V, Ksenofontov V. A, Masilov A. A & Sadanov E.V (2013). Formation of Interstitial Atoms in Surface Layers of Helium-Implanted Tungsten. *Technical Physics Letters* 39 (11): 960‑ 63. https://doi.org/10.1134/S1063785013110035.

Fajardo, R.V (2016). Calculation of the Equilibrium Lattice Constants and Stable Lattice Structure of Nickel. *Introduction to Density Functional Theory Calculations*.

Felfer P, Ott B, Monajem M, Dalbauer V, Heller M , Josten J & Macaulay C (2022). An Atom Probe with Ultra-Low Hydrogen Background. *Microscopy and Microanalysis* 28 (4): 1255‑ 63. https://doi.org/10.1017/S1431927621013702.

Gault B, Chiaramonti A, Cojocaru-Mirédin O, Stender P, Dubosq R, Freysoldt C, Makineni S. K, Li T, Moody M & Cairney J.M (2021). Atom Probe Tomography. *Nature Reviews Methods Primers* 1 (1): 51. https://doi.org/10.1038/s43586-021-00047-w.

Gemma R., Al-Kassab T, Kirchheim R & Pundt A (2009). APT Analyses of Deuterium-Loaded Fe/V Multi-Layered Films. *Ultramicroscopy* 109 (5): 631‑ 36. https://doi.org/10.1016/j.ultramic.2008.11.005.

Geuser, F. de (2006). Interprétation et traitement des données de sonde atomique tomographique: application à la precipitation dans les Al-Mg-Si.

HACHET, G., OUDRISS, A., BARNOUSH, A., MILET, R., WAN, D., METSUE, A. & FEAUGAS, X. (2020). The influence of hydrogen on cyclic plasticity of oriented nickel single crystal. Part I: Dislocation organisations and internal stresses. *International Journal of Plasticity* **126**, 102611.

Hölzl J, Schulte F.K & Wagner H, éd. (1979). *Solid Surface Physics*. Springer Tracts in Modern Physics 85. Berlin Heidelberg: Springer.

Houard J, Vella A, Vurpillot F & Deconihout B (2011). Three-Dimensional Thermal Response of a Metal Subwavelength Tip under Femtosecond Laser Illumination. *Physical Review B* 84 (3): 033405. https://doi.org/10.1103/PhysRevB.84.033405.

Hyde J.M, Cerezo A, Setna R.P, Warren P.J & Smith G.D.W (1994). Lateral and Depth Scale Calibration of the Position Sensitive Atom Probe. *Applied Surface Science* 76‑ 77 (mars): 382‑ 91. https://doi.org/10.1016/0169-4332(94)90371-9.

Kellogg G. L & Panitz J. K. G (1980). A Direct Observation of the Trapping of Deuterium Ions at a Grain Boundary in Tungsten. *Applied Physics Letters* 37 (7): 625‑ 27. https://doi.org/10.1063/1.91999.

Klaes B (2020). Nouvelle méthode d'imagerie 3D et d'analyse quantitative des défauts ponctuels et amas de défauts pour l'étude du vieillissement des matériaux.

Koyama M, Akiyama E, Lee Y-K, Raabe D & Tsuzaki K (2017). Overview of Hydrogen Embrittlement in High-Mn Steels. *International Journal of Hydrogen Energy* 42 (17): 12706‑ 23. https://doi.org/10.1016/j.ijhydene.2017.02.214.

Lee J-Y & Lee J-L (1987). A Trapping Theory of Hydrogen in Pure Iron. *Philosophical Magazine A* 56 (3): 293‑ 309. https://doi.org/10.1080/01418618708214387.

Lefebvre-Ulrikson W, éd. (2016). *Atom Probe Tomography: Put Theory into Practice*. London: Academic Press.

Lin Y-C, McCarroll I. E, Lin Y-T, Chung W-C, Cairney J. M & Yen H-W (2020). Hydrogen Trapping and Desorption of Dual Precipitates in Tempered Low-Carbon Martensitic Steel. *Acta Materialia* 196 (septembre): 516‑ 27. https://doi.org/10.1016/j.actamat.2020.06.046.

Loi S. T, Gault B, Ringer S. P, Larson D. J & Geiser B. P (2013). Electrostatic Simulations of a Local Electrode Atom Probe: The Dependence of Tomographic Reconstruction Parameters on Specimen and Microscope Geometry. *Ultramicroscopy* 132 (septembre): 107‑ 13. https://doi.org/10.1016/j.ultramic.2012.12.012.

Lucasson P & Lucasson A (1963). Fonctions de potentiel interatomiques déduites d'énergies. Seuil de déplacements. *Journal de Physique* 24 (7): 503‑ 7. https://doi.org/10.1051/jphys:01963002407050300.

Maxwell J.C (1860). Illustrations of the dynamical theory of gases.

Mazilov A A. (2015). DETERMINATION OF THE SPECTRA OF ION He AND H2 BOMBARDMENT OF AUTOEMITTER SURFACE.

McCarroll I.E, Bagot P.A.J, Devaraj A, Perea D.E & Cairney J.M (2020). New Frontiers in Atom Probe Tomography: A Review of Research Enabled by Cryo and/or Vacuum Transfer Systems. *Materials Today Advances* 7 (septembre): 100090. https://doi.org/10.1016/j.mtadv.2020.100090.

Miller M. K & Forbes R. G (2014). *Atom-Probe Tomography*. Boston, MA: Springer US. https://doi.org/10.1007/978-1-4899-7430-3.

Mouton I, Breen A. J, Wang S, Chang Y, Szczepaniak A, Kontis P, Stephenson L.T, Raabe D, Herbig M, Britton TB & Gault B. (2019). Quantification Challenges for Atom Probe Tomography of Hydrogen and Deuterium in Zircaloy-4. *Microscopy and Microanalysis* 25 (2): 481‑ 88. https://doi.org/10.1017/S143192761801615X.

Muller E. W (1951). Das Feldionenmikroskop. *Zeitschrift for Physik* 131 (1): 136‑ 42. https://doi.org/10.1007/BF01329651.

Müller E. W & Bahadur K (1956). Field Ionization of Gases at a Metal Surface and the Resolution of the Field Ion Microscope. *Physical Review* 102 (3): 624‑ 31. https://doi.org/10.1103/PhysRev.102.624.

Panayi P, Clifton P.H, Lloyd G, Shellswell G & Cerezo A (2006). A Wide Angle Achromatic Reflectron for the Atom Pprobe. In *2006 19th International Vacuum Nanoelectronics Conference*, 63‑ 63. Guilin, China: IEEE. https://doi.org/10.1109/IVNC.2006.335353.

Paulini J, Klein T & Simon G (1993). Thermo-Field Emission and the Nottingham Effect. *Journal of Physics D: Applied Physics* 26 (8): 1310‑ 15. https://doi.org/10.1088/0022-3727/26/8/024.

Pressouyre G. M (1979). A Classification of Hydrogen Traps in Steel. *Metallurgical Transactions A* 10 (10): 1571‑ 73. https://doi.org/10.1007/BF02812023.

Rousseau L, Normand A, Morgado F. F, Stephenson L, Gault B, Tehrani K & Vurpillot F (2020). Dynamic Effects in Voltage Pulsed Atom Probe. *Microscopy and Microanalysis* 26 (6): 1133‑ 46. https://doi.org/10.1017/S1431927620024587.

Sandrock G (1999). A Panoramic Overview of Hydrogen Storage Alloys from a Gas Reaction Point of View. *Journal of Alloys and Compounds* 293‑ 295 (décembre): 877‑ 88. https://doi.org/10.1016/S0925-8388(99)00384-9.

Schmidt R, Schlereth M, Wipf H, Assmus W & Mullner M (1989). Hydrogen Solubility and Diffusion in the Shape-Memory Alloy NiTi. *Journal of Physics: Condensed Matter* 1 (14): 2473‑ 82. https://doi.org/10.1088/0953-8984/1/14/003.

So K. H, Kim J.S, Chun Y. S, Park K-T, Lee Y-K & Lee C. S (2009). Hydrogen Delayed Fracture Properties and Internal Hydrogen Behavior of a Fe–18Mn–1.5Al–0.6C TWIP Steel. *ISIJ International* 49 (12): 1952‑ 59. https://doi.org/10.2355/isijinternational.49.1952.

Sofronis P (2006). Viable Mechanisms of Hydrogen Embrittlement—A Review. In *AIP Conference Proceedings*, 837:64‑ 70. Uppsala (Sweden): AIP. https://doi.org/10.1063/1.2213060.

Song Y, Han Z, Chai M, Yang B, Liu Y, Cheng G, Li Y & Ai S (2018). Effect of Cementite on the Hydrogen Diffusion/Trap Characteristics of 2.25Cr-1Mo-0.25V Steel with and without Annealing. *Materials* 11 (5): 788. https://doi.org/10.3390/ma11050788.

Straub H. C, Renault P, Lindsay B. G, Smith K. A & Stebbings R. F (1996). Absolute Partial Cross Sections for Electron-Impact Ionization of H 2 , N 2 , and O 2 from Threshold to 1000 EV. *Physical Review A* 54 (3): 2146‑ 53. https://doi.org/10.1103/PhysRevA.54.2146.

Sundell G, Thuvander M & Andrén H-O (2013). Hydrogen Analysis in APT: Methods to Control Adsorption and Dissociation of H2. *Ultramicroscopy* 132 (septembre): 285‑ 89. https://doi.org/10.1016/j.ultramic.2013.01.007.

Takahashi J, Kawakami K & Kobayashi Y (2018). Origin of Hydrogen Trapping Site in Vanadium Carbide Precipitation Strengthening Steel. *Acta Materialia* 153 (juillet): 193‑ 204. https://doi.org/10.1016/j.actamat.2018.05.003.

——— 2019. Application of Atom Probe Tomography to Fundamental Issues of Steel Materials. *Surface and Interface Analysis* 51 (1): 12‑ 16. https://doi.org/10.1002/sia.6535.

Takahashi J, Kawakami K, Kobayashi Y & Tarui T (2010). The First Direct Observation of Hydrogen Trapping Sites in TiC Precipitation-Hardening Steel through Atom Probe Tomography. *Scripta Materialia* 63 (3): 261‑ 64. https://doi.org/10.1016/j.scriptamat.2010.03.012.

Tsong T T (1978). FIELD ION IMAGE FORMATION. *Surface Science* 70: 211‑ 33.

Tweddle D, Hamer P, Shen Z, Markevich V. P, Moody M. P & Wilshaw P. R (2021). Direct Observation of Hydrogen at Defects in Multicrystalline Silicon. *Progress in Photovoltaics: Research and Applications* 29 (11): 1158‑ 64. https://doi.org/10.1002/pip.3184.

Vurpillot F, Houard J, Vella A & Deconihout B (2009). Thermal Response of a Field Emitter Subjected to Ultra-Fast Laser Illumination. *Journal of Physics D: Applied Physics* 42 (12): 125502. https://doi.org/10.1088/0022-3727/42/12/125502.

Vurpillot F, Lardé R, Klaes B & Da Costa G (2023). « Automated Tomography Field Ion Microscope ». US011791129B2.

Walck S. D & Hren J. J (1984). FIM/IAP/TEM STUDIES OF HYDROGEN IN METALS. *Le Journal de Physique Colloques* 45 (C9): C9-355-C9-360. https://doi.org/10.1051/jphyscol:1984959.

Wimmer E, Wolf W, Sticht J, Saxe P, Geller C. B, Najafabadi R & Young G. A (2008). Temperature-Dependent Diffusion Coefficients from *Ab Initio* Computations: Hydrogen, Deuterium, and Tritium in Nickel. *Physical Review B* 77 (13): 134305. https://doi.org/10.1103/PhysRevB.77.134305.

Yoo S-H, Kim S-H, Woods E, Gault B, Todorova M & Neugebauer J (2022). Origins of the Hydrogen Signal in Atom Probe Tomography: Case Studies of Alkali and Noble Metals. *New Journal of Physics* 24 (1): 013008. https://doi.org/10.1088/1367-2630/ac40cd.